PCCP

Accepted Manuscript

ROYAL SOCIETY OF CHEMISTRY

www.rsc.org/pccp

Cite this: DOI: 10.1039/c0xx00000x

www.rsc.org/xxxxxx

ARTICLE TYPE

Plasmon-mediated photocatalytic activity of wet-chemically prepared ZnO nanowire arrays

Thang Duy Dao[*†‡§], Gui Han[*#], Nono Arai[*], Toshihide Nabatame[*], Yoshiki Wada[†], Chung Vu Hoang[*], Masakazu Aono[*†], and Tadaaki Nagao[*†]

We report on measurements and simulations of the efficient sunlight-driven and visible-active photocatalysts composed of plasmonic metal nanoparticles and ZnO nanowire (NW) arrays fabricated via an all-wet-chemical route. Because of the coupling between the ZnO dielectric response and the excitation of the Ag or Au nanoparticles, efficient electronic excitation can be induced in the vicinity of the metal-ZnO interfaces because optically-excited plasmonic particles can not only concentrate the electromagnetic field at the ZnO/particle interface, but also act as efficient sources of plasmonic hot electrons to be injected into the conduction band of the ZnO catalyst. The catalytic activities of the fabricated ZnO NWs are examined by photodegradation of methylene blue and by photocurrent measurements in a photovoltaic configuration. Numerical electromagnetic simulations were used to understand the behavior of the light on the nanometer-scale to clarify the catalytic enhancement mechanisms in both the ultraviolet (UV) and visible (VIS) regions. In addition, simulation result indicated that a near-surface normal but slightly tilted ZnO NW arrays geometry would provide an increased optical path length and enhanced multiple scattering and absorption processes arising from the localized surface plasmon resonances of the nanoparticles. The results obtained here clarify the role of the plasmon resonance and provide us with useful knowledge for the development of metal-oxide nano-hybrid materials for solar energy conversion.

[*] *International Center for Materials Nanoarchitectonics, National Institute for Materials Science, 1-1 Namiki, Tsukuba, Ibaraki 305-0044, Japan.*

[†] *Environment and Energy Materials Division, National Institute for Materials Science, 1-1 Namiki, Tsukuba, Ibaraki 305-0044, Japan.*

[‡] *CREST-JST, 4-1-8 Honcho, Kawaguchi, Saitama 332-0012 Japan.*

[§] *Graduate School of Materials Science, Nara Institute of Science and Technology, 8916-5 Takayama, Ikoma, Nara 630-0192, Japan.*

[#] *School of Chemistry & Chemical Engineering, Shouxihu Campus, Yangzhou University, Jiangsu Province, China, 225002*

E-mail: Dao.DuyThang@nims.go.jp; NAGAO.Tadaaki@nims.go.jp; AONO.Masakazu@nims.go.jp

Cite this: DOI: 10.1039/c0xx00000x

www.rsc.org/xxxxxx

ARTICLE TYPE

1. Introduction

Artificial photosynthesis and photocatalysis have become central topics in energy and environmental research as two of the most promising clean processes for conversion of solar energy into chemical energy. Metal-oxide catalysts such as TiO_2-based self-cleaning house paint and window coatings have been studied extensively. While remarkable successes have been reported in the applications of these materials to date, most semiconductor catalysts have optical bandgaps in the ultraviolet (UV) region, such as TiO_2 (3.2 eV)[1], ZnO (3.37 eV)[2], and $SrTiO_3$ (3.2 eV)[3], which are too high to allow efficient use of solar energy in the visible (VIS) and infrared (IR) regions. Recent advances leading to improvements in catalytic efficiency and development of VIS-IR active catalysts have led to numerous challenges in the fields of photocatalysis and nanophotonics.

Recently, plasmonic nanostructures have demonstrated great potential for applications in optics, photonics and optoelectronics, based on their extreme enhancement and nanoscale confinement of electromagnetic fields in the vicinity of their surfaces. Similar features have also been realized to enhance the efficiency of catalytic materials[4–7] by near-field enhancement[8–11] where the strong electric field is extremely amplified at metal-semiconductor surface, resulting in efficient absorption of photons. Especially, the excited plasmons can also provide sufficient energy to inject hot electrons from metal nanostructures into semiconductor[12–15], resulting in visible light photocatalysis even with UV bandgap materials such as Au-TiO_2[4,16–20], Ag-TiO_2[21,22], and Au- $SrTiO_3$[23].

Among the various available photocatalysts, zinc oxide (ZnO) has been widely studied as a highly efficient material[24–33] because of its natural abundance, inexpensive fabrication processes, rendering, ZnO as an promising photocatalyst beside TiO_2 and $SrTiO_3$. In particular, ZnO nanowires (NWs) have been studied extensively as excellent catalysts because of their high surface area and increased optical path-length mediated by light scattering and interference[28–33]. However, because of its wide bandgap, the photocatalytic activity of ZnO NWs is limited mainly under UV light, making the challenger for the use of ZnO in the solar-assisted photocatalysis application. To improve photocatalytic activity of ZnO NWs, beside the bandgap modification by doping of ZnO NWs with metal ions[30,34–36], nanometals were also chosen as the co-catalysts materials for the enhancement of the charge separation[29,37,38] or as the plasmonic materials for the near field enhancement and hot-electron injection[32,39,40]. The catalytic activity of plasmonic nanometals-ZnO NWs heterostructures can be improved in both UV and VIS regions, however, the enhancement factor as well as the efficiency enhancement are dependent on the structure morphology and electric field direction. Deeper understanding for both UV and VIS catalytic enhancements of the AgNP-ZnO and AuNP-ZnO NWs hybrids based on measurement and electromagnetic field simulation are needed.

In this work, we propose an effective metal-oxide hybrid nano-architecture and a simple low-cost fabrication method for this nano-architecture, together with experimental demonstration of visible photocatalytic activity in this structure. It is also interesting to see the extent to which numerical analysis of the electromagnetic field on the nanometer scale can explain the improvement in the chemical properties of the proposed nanostructures. The proposed nanomaterials here are metal nanoparticles (NPs)-loaded ZnO nanowires, which exhibit greatly improved catalytic activity in the visible region. The fabricated catalyst consists of a nearly-vertical ZnO nanowire array that is hydrothermally grown on transparent conductive oxides (TCOs), *e.g.* on fluorine-doped tin oxide (FTO) or on indium tin oxide (ITO)-coated glass substrates. The plasmonic Ag and Au NPs were prepared separately and attached to the ZnO nanowires to form AgNP-loaded ZnO or AuNP-loaded ZnO catalysts. The photodegradation of methylene blue molecules under solar illumination was examined. The catalytic activity of the metal-NP-loaded-ZnO surfaces was found to be 2–3 times higher than that of pure ZnO NWs. A photoelectrochemical (PEC) cell in photovoltaic configuration with NP-loaded ZnO NWs photoanodes showed clear photocatalytic activity in the VIS region, while negligible activity was observed in the case of a pure ZnO NWs photoanode. In addition, numerical electromagnetic field simulations were used to investigate the optical properties of these materials and to understand the mechanism of catalytic activity enhancement by addition of plasmonic metal particles to ZnO NWs. The numerical electromagnetic simulations were performed to clarify the absorption characteristics of the catalysts in the visible region that were associated with plasmonic extinction of the AgNPs and AuNPs. The simulated electric field distributions showed strong electric field concentrations at the interfaces between the metal NPs and ZnO under both UV (near the ZnO bandgap) and VIS (at localized surface plasmon resonance) excitations. In particular, at plasmon resonance in the VIS region in the AgNP-ZnO case (ca. 450 nm) and in the AuNP-ZnO case (ca. 560 nm), the electric fields were found to be enhanced by 20 times, which increases the probability of internal photoemission to generate hot electrons that can overcome the Schottky barrier and be injected into the ZnO conduction band to functionalize the material as a VIS-active photocatalyst.

2. Experiments and simulation

2.1. Preparation and characterization of plasmonic AuNPs- and AgNPs- ZnO NWs hybrids

ZnO NW arrays were synthesized on transparent conductive oxide (FTO or ITO) substrates (1×2 cm) by the hydrothermal method[41]. The fabricated ZnO NW arrays were then washed in de-ionized water and in ethanol, and were then annealed at 400°C in ambient air for 1 h to enhance the crystallinity of the ZnO crystals and the shallow donor concentrations[42,43]. A colloidal suspension of AgNPs (average diameter of 10 nm) was synthesized by adding sodium tetrahydroborate ($NaBH_4$, Wako) to reduce the ionic silver ($AgNO_3$, Wako) and stabilize the silver nanoparticles[44]. The aqueous solution of AuNPs (average diameter of 13 nm) was synthesized by reducing ionic gold (hydrogen tetrachloroaurate (III) tetrahydrate ($HAuCl_4$), Wako) using anhydrous trisodium citrate ($C_6H_5Na_3O_7$, Wako)[45]. To prepare AgNP-ZnO and AuNP-ZnO hybrids, 200 µl of aqueous solutions of AuNPs and AgNPs with particle density of

5×10^{12}.ml^{-1} were entirely drop on to 1×2 cm ZnO NWs substrates. The samples were then kept in a plastic box for 10 h. The nanoparticles with negative surface charge could be adsorbed on the ZnO NWs with positive surface charges[46,47] by electrostatic force. The metal NPs-ZnO samples were then washed in de-ionized water to remove the excess AgNPs and AuNPs and then dried and thermally treated at 150°C in air (with low oxygen content to prevent oxidation of the silver) for 1 h to stabilize the metal-ZnO interfaces. The density of NPs adsorbed on ZnO NWs was estimated by analyzing SEM images. As the results, the coverage of NPs on ZnO (the ratio between projected areas of NPs on the total surface area of ZnO NWs) was found to be approximately 15%. It should be noted that the density of metal NPs adsorbed on ZnO NWs can be controlled by changing the adsorption time and the volume of the dropped NPs solutions.

The nano-morphology of the catalysts was characterized using a field emission scanning electron microscope (FE-SEM, Hitachi SU8000, 10 kV operating voltage), an X-ray diffractometer (XRD, Rigaku Rint 2000, Cu Kα) and a transmission electron microscope (TEM, JEOL JEM-2100F, 200 kV accelerating voltage). The 2θ scanning range of the XRD was from 30° to 50° with a scanning speed of 0.2° min^{-1}. The transmittance of each sample was examined using a UV-VIS spectrometer (Jasco V-570) at room temperature, and the photoluminescence was measured using a fluorescence microscope (Horiba Jobin-Yvon) with a 325 nm He-Cd excitation laser source. The investigation of photodegradation in water was performed using NPs-ZnO NWs photocatalysts, in which a 2 ml solution of MB molecules with a concentration of 10^{-5} M in water was used. For the photoelectric conversion measurements, a simple PEC cell was used, with photoanodes made from AgNP-ZnO and AuNP-ZnO NWs hybrids. These metal NPs-ZnO NW arrays were grown on ITO substrates and were connected to high-purity copper wire using silver paste, and an insulating epoxy was then used to cover all excess ITO surfaces on the edge of the ITO glass to prevent short-circuit currents. The PEC cell measurements were carried out in a photovoltaic configuration with the catalyst photoanodes, a Pt zigzag wire acting as the counter electrode, and Na_2SO_4 solutions (0.5 M) acting as the electrolyte. A standard AM 1.5 G solar simulator (Jasco Otentosun - IV 5) with power density of 100 mW·cm^{-2} was used as the sunlight source for both the PEC cell and photodegradation experiments. For measurements under VIS irradiation, an additional optical filter was combined with the solar simulator to eliminate the UV light.

2.2. Electromagnetic simulation of plasmonic AuNPs- and AgNPs- ZnO NWs hybrids

The numerical electromagnetic simulations of the transmission spectra for the AgNP- and AuNP-loaded-ZnO NW arrays were performed systematically using the rigorous coupled-wave analysis (RCWA) method (Diffractmod, Rsoft). The real-space electric-field distributions on the nanostructures under external excitation fields were calculated using the finite-difference time-domain (FDTD) method (Fullwave, Rsoft). The geometries of the nano-objects used for the simulations were hexagonal cylinder shapes for the ZnO nanowires (50–100 nm in diameter) and spherical shapes for the Ag and Au particles. The diameters of the Au and Ag particles varied from 10 up to 20 nm, but no significant difference was observed in the results for the proposed systems. The simulation domain size and the grid size used to set the material boundary conditions were chosen to guarantee conversion of the simulated results. The dielectric functions of Ag, Au, ZnO, and water were taken from the literature[48,49]. A real part of 1 and an imaginary part of 0 for the dielectric function of air were used in the calculations.

3. Results and discussion

3.1. Crystallinity and morphology of the fabricated nanostructures

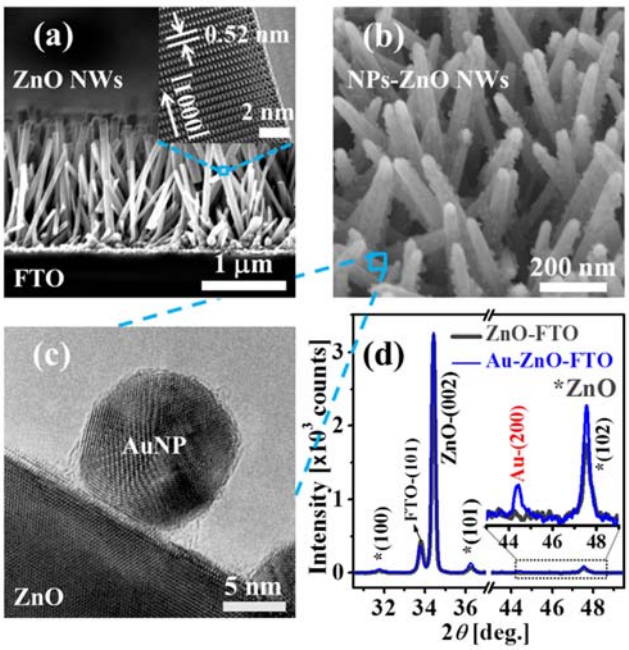

Fig. 1 (a) Cross-sectional SEM image of a ZnO NW arrays and a high-resolution TEM image (inset) of a single ZnO NW with [0001] growth orientation. (b) Tilted-view SEM image of an AuNP-ZnO NW array. (c) TEM image of an AuNP on the ZnO NW surface. (d) XRD patterns of an AuNP-coated (blue curve) and non-coated (gray curve) ZnO NW arrays. The inset in (d) shows an enlarged scale of XRD patterns from 43-49 degree.

Figure 1a presents a cross-sectional SEM image of a ZnO NW arrays grown on an FTO-glass substrate with an average wire length of 1 μm, wire diameter of 50 nm, and wire density of 2×10^{10} cm^{-2}. A high-resolution TEM image of a single ZnO NW (the inset in Fig. 1a) shows very high crystalline quality with a [0001] growth orientation. A tilted-view SEM image of the AuNP-ZnO NW arrays (Fig. 1b) shows that the particles are uniformly attached to the surfaces of the ZnO NWs. In addition, a high-resolution TEM image of an NP-loaded NW (Fig. 1c) shows good contact between the metal-NP and the ZnO semiconductor. Figure 1d shows XRD patterns for the bare ZnO NWs on the FTO substrate (gray curve) and the AuNP (blue curve); both curves exhibit ZnO diffraction peaks that are in good agreement with JCPDS card No 36-1451 for bulk ZnO with a hexagonal wurtzite structure. In addition, a strong peak at 34.39° of the ZnO (002) plane shows that the nanowires are well oriented and are of high crystalline quality. Also, the XRD pattern for the AuNP-ZnO NWs exhibits an additional diffraction peak (the inset in Fig. 1d), which is ascribed to the (200) plane of the AuNP. We also characterized the AgNP-ZnO NW arrays using the same TEM and XRD observations and confirmed that they exhibit similar morphology and crystallinity to the AuNP-loaded ZnO NW arrays.

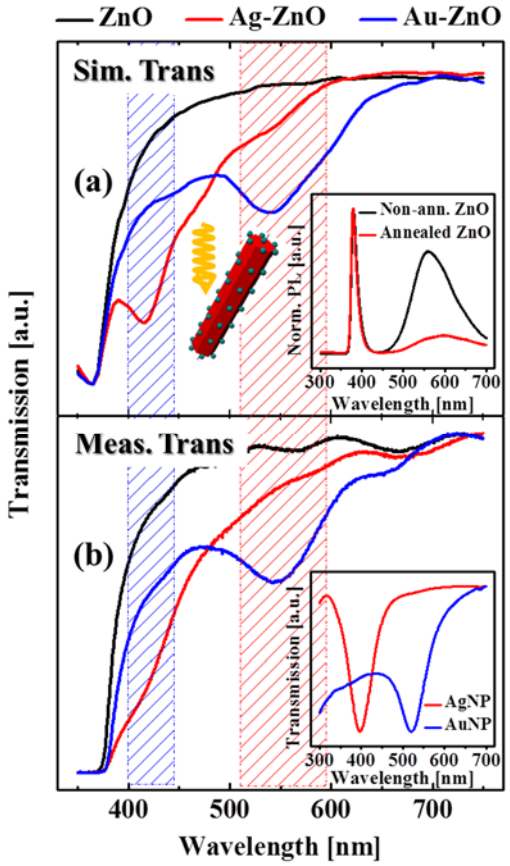

Fig. 2 (a) Simulation and (b) measurement results for the transmission spectra of the bare ZnO NW arrays (black curve), the AgNP-loaded ZnO NWs (blue curve), and AuNP-loaded ZnO NWs (red curve). The insets in (a) show a unit cell simulation model, including NPs on the ZnO surface with a tilt angle of 30° with respect to the incident light direction, and the photoluminescence spectra of the ZnO nanowires before and after annealing at 400°C. The inset in (b) shows the experimental transmission spectra of the original AgNP and AuNP suspensions in water.

3.2. Optical properties

To clarify the optical properties of the metal NP-loaded-ZnO catalyst, we first simulated the transmission spectra and then compared the results obtained with the UV-VIS spectra of the materials. Figure 2 presents the simulation (Fig. 2a) and measurement (Fig. 2b) results for the transmission of the ZnO NW arrays with and without the plasmonic metals, with air as the surrounding medium. The model geometry is shown as an inset in Fig. 2a. For this simulation, the illuminating light was at an angle of incidence of 30° with respect to the nanowire axis, and this will be discussed in greater detail later in the paper. The inset in Fig. 2b shows the transmission spectra of the AgNP and AuNP suspensions in water, which exhibit plasmon resonances at 390 nm and 523 nm, respectively. The agreement between the results of the simulations and those of the experiments is very good. The results indicate high transparency for wavelengths above 400 nm in the case of bare ZnO NWs (black curve), while in the presence of plasmonic NPs, an absorption feature around 415 nm for the AgNP-ZnO case (red curve) and a wide absorption band from 450 nm to 630 nm for the AuNP-ZnO case (blue curve) are observed. Because of the dielectric screening from the ZnO, the plasmon resonances of the NPs are slightly red-shifted when the NPs are attached to the ZnO NWs. In the presence of the plasmonic metals, the optical densities of the NP-loaded-ZnO NW arrays increased in the VIS region, which is the requirement for a photocatalyst that operates under solar illumination.

The ZnO NW crystal quality was improved by an annealing process and was evaluated by photoluminescence measurements, as shown in the inset in Fig. 2a. As we can clearly see, broad VIS emission (ca. 500-700 nm) was reduced by the annealing process, which is attributed to an increase in the shallow donor levels[42], and results in a high donor concentration and improved crystallinity and conductivity for the ZnO catalyst.

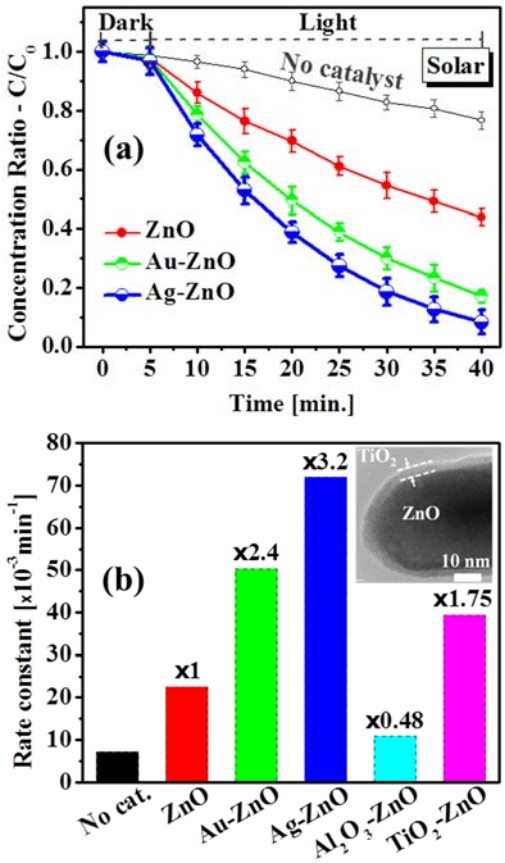

Fig. 3 Photodegradation of methylene blue (MB) molecules in water under full-spectrum sunlight illumination. (a) Reductions in the MB concentrations are shown without a catalyst (gray curve), and in the presence of bare ZnO NW arrays (red curve), AuNP-ZnO NW arrays (green curve) and AgNP-ZnO NW arrays (blue curve). Error bars represent the standard deviation for three independent experiments. (b) The MB photodegradation rate constants in the presence of the different catalysts are shown. The inset shows a TEM image of a thin TiO_2 layer-coated ZnO NW catalyst.

3.3. Photodegradation of MB in water

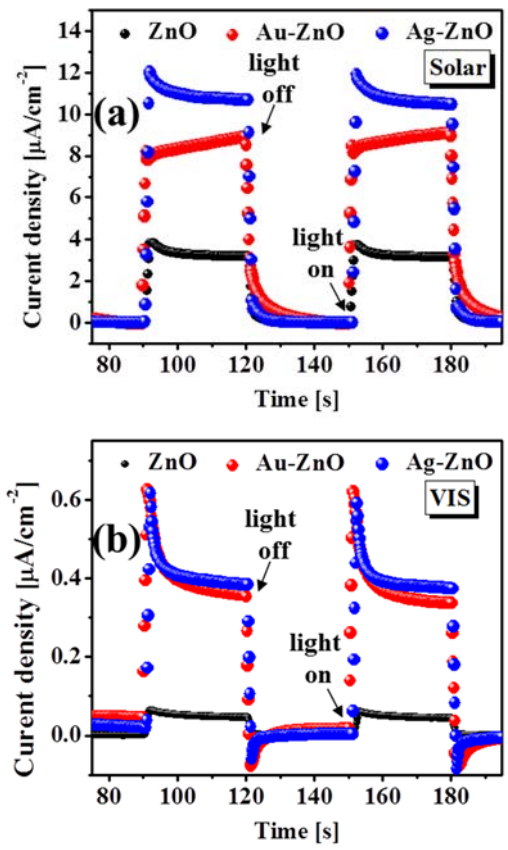

Fig. 4 Photocurrent densities of ZnO NWs and NP-ZnO NW photoanodes of the PEC cell in photovoltaic configuration, (a) under full-spectrum sunlight illumination with power density of 100 mW·cm^{-2} (standard AM 1.5G filter), and (b) under visible light illumination (wavelength in the 400–900 nm range with power density of 33 mW·cm^{-2}).

One possible use of the oxide photocatalyst is in the decomposition of unwanted pollutant molecules and toxic molecules in water under illumination by sunlight. The catalytic activity of the plasmonic metal-loaded ZnO NW catalysts was investigated via the photodegradation (reduction) of the methylene blue (MB) molecule under full-spectrum sunlight illumination (standard AM 1.5G solar simulator). The solution of MB (deep blue) transforms into leucomethylene blue (transparent) as the MB reduction occurs. Figure 3a shows the photodegradation plot of the MB molecules in water determined by monitoring the reduction of the MB concentration under solar illumination[50]. Initially, the degradation of the MB solution was evaluated without any illumination to see the chemical process in the dark and the instrument function of the measurement system that constitutes the background spectrum. After illumination, the MB concentration is slowly reduced by photoreaction without any catalyst. In contrast, in the presence of the ZnO catalysts, the molecules are dramatically reduced by the photocatalytic process. In particular, by loading the plasmonic NPs onto the ZnO, the catalytic activities of AuNP-ZnO and AgNP-ZnO NW hybrids become much higher than that of the pristine ZnO NWs. For further quantitative investigation using first-order Langmuir-Hinshelwood kinetics[51], we evaluated the apparent MB reduction rate in the presence of the catalysts, as shown in Fig. 3b. When compared with the pristine-ZnO NW case with its rate constant of 22.5×10^{-3} min^{-1}, the photocatalytic activity of the NP-loaded ZnO catalysts is enhanced remarkably by 2.4 and 3.2 times in the AuNP-ZnO and AgNP-ZnO hybrids, respectively.

For further investigation, the ZnO NW surfaces were also capped by ultra-thin oxide layers (thickness of 4 nm) of Al_2O_3 or anatase TiO_2 to determine the effects of the oxide surfaces. The oxide layers were deposited by atomic layer deposition. As shown in Fig. 3b, the Al_2O_3-coated ZnO NW arrays show little catalytic activity, as expected from the bulk properties of the material and its wide bandgap energy (8 eV). In contrast, the anatase TiO_2-coated ZnO NW arrays show improved catalytic activity in comparison to that of pure-ZnO NWs, which is due to improvement in the charge transport caused by removal of the ZnO trap states[52] during formation of the TiO_2 shell layer, along with the inherent catalytic activity of TiO_2. However, the catalytic activity of TiO_2-coated ZnO NWs is still far smaller than that of the NP-loaded ZnO NWs, thus highlighting the dramatic enhancement of the catalytic activity produced by the plasmonic NPs. The above results can be summarized as follows. The catalytic activity is associated with the ZnO surface chemistry, which is higher than that of Al_2O_3 and lower than that of TiO_2, and the activity can be improved dramatically to a level that surpasses by far the activity of the TiO_2 surface alone by a factor of two to three by decoration with metal NPs. It is also notable that these NPs-ZnO NWs photocatalysts can be reused many times with high stability. For example, after the catalysts were used, they were rinsed several times with pure water and dried in ambient air. This simple cleaning method allows us to use them more than ten more times with stable catalytic activity.

3.4. PEC measurements

To further understand the role of the metal NPs in the photocatalytic activity, we have measured the photocurrents using the PEC cell under illumination by the solar simulator. We investigated the photocatalytic activity of the plasmonic NP-loaded-ZnO NW arrays by using them as the photoanodes in our PEC cell, together with a cathode made from Pt zigzag wire. A 0.5 M sodium nitrate solution (pH~7) was used as the electrolyte. The photovoltaic configuration for the PEC cell was used, meaning that no bias voltage was applied during the photocurrent measurements. Figure 4 presents the photocurrent density of the PEC with and without illumination. Under standard 100 mW·cm^{-2} solar light, as shown in Fig. 4a, the average photocurrents were 8.5 and 11 μA·cm^{-2} for the two photoanodes made from AuNP- and AgNP-loaded ZnO NWs hybrids, respectively, while it is only 3.2 μA·cm^{-2} in the pure ZnO NW photoanode case. The results clearly show that by using NP-loaded ZnO NW catalysts, the photocatalytic activity was enhanced by 2.5–3.5 times. To investigate the activity enhancement mechanism, we measured the photocurrent of the PEC cell under pure VIS-IR irradiation (400–900 nm) while using an optical filter to cut all UV light (Fig. 4b). Under VIS light illumination, little photocurrent was generated in case of the pure ZnO NWs, while the photocurrents in cases of the AgNP- and AuNP-loaded ZnO NWs rise steeply to more than 0.6 μA·cm^{-2}. It should be emphasized here that even under VIS light irradiation, the photoelectric conversion process is operative in the presence of the plasmonic-metal NPs loaded on the ZnO NW catalysts.

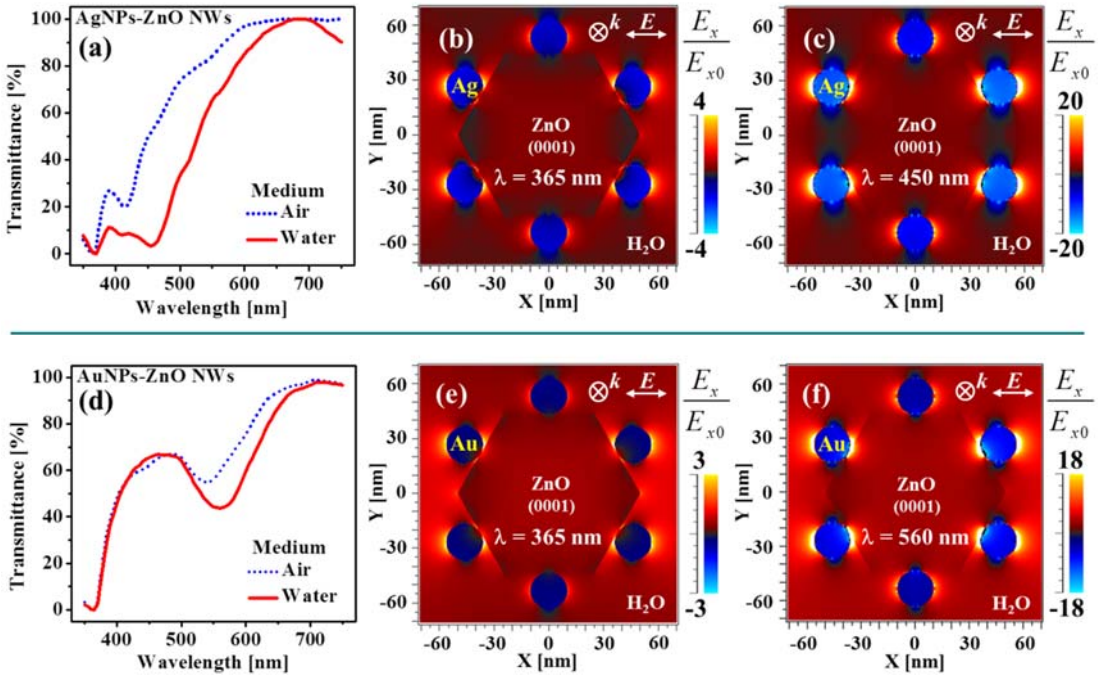

Fig. 5 Simulated transmittance (red curves) of (a) AgNP-ZnO NW catalysts and (d) AuNP-ZnO NW catalysts in the realistic working medium of water. The simulated electric field distribution around the plasmonic metal-semiconductor catalyst shows that strong E-field enhancement and hot spots located at the metal-semiconductor interface would provide smart potential for hot electrons: These distributions are shown for AgNP-ZnO NWs in (b) under UV excitation at 365 nm with E-field enhancement of 4, and in (c) under visible excitation of plasmon resonance at 450 nm with strong E-field enhancement of 20; and for AuNP-ZnO NWs in (e) under UV excitation at 365 nm with E-field enhancement of 3, and in (f) under visible excitation of plasmon resonance at 560 nm with strong E-field enhancement of 18.

3.5. Electric field enhancement and discussion

To determine both the optical properties and the enhancement mechanism of these plasmonic metal-loaded ZnO catalysts, the electric field (E-field) distributions around the nano-objects were calculated using FDTD simulations. These simulations were performed using water as the surrounding medium, which reproduces the experimental conditions of the catalyst. First, under UV excitation at the optical band-gap energy of 360 nm ZnO NWs, the E-field enhancement near the Au-ZnO and Ag-ZnO interfaces were found to be three and four times larger, respectively, when compared with the E-field of the incident light. This enhancement in the UV range in particular, corresponding to the optical band-gap of ZnO, can contribute remarkably to the efficiency of the photocatalysts. In addition, the excitation energy in the UV range is larger than the thresholds of the interband transitions of both Ag and Au, which can lead to excitation of electrons far below the Fermi level, *e.g.*, the interband transition from the *d*-band to the *sp*-band in gold. In this case, the photogenerated holes in the *d*-band may act as hot holes and contribute to the injection current[53]. However, under VIS excitation at the plasmon resonances at 450 nm for Ag-ZnO (in water) and 560 nm for Au-ZnO (in water), the E-field enhancement factors were found to be as high as 18 and 20 times for Au-ZnO and Ag-ZnO, respectively. These concentrated E-fields are mostly located at the interfaces between the metal NPs and ZnO, and also penetrate slightly into the ZnO subsurface, indicating the concentration of the photon energy into a tiny space at the NP/ZnO interface. With a Schottky barrier at the heterojunction between a metal with a work function that is smaller or larger than the vacuum electron affinity of a p-type or n-type semiconductor, respectively, the quantum transition probability of the electrons with sufficient energy to overcome the barrier is given by:[12,54]

$$\eta_i \approx C_F \frac{(h\nu - q\phi_B)^2}{h\nu};$$

where C_F is the device-specific Fowler emission coefficient, $q\phi_B$ is the Schottky barrier energy and $h\nu$ is the photon energy. Here, in the case of junctions between Ag with work function of 4.26–4.74 eV[55] or Au with work function of 5.1–5.47 eV[55] and native n-type ZnO NWs[56] with vacuum electron affinity of 4.19–4.5 eV[57],, the Schottky barriers were estimated to be in the ranges from 0.1–0.5 eV for the Ag-ZnO junction and 0.5–1.3 eV for the Au-ZnO junction, which are far smaller than the plasmon energy of Ag-ZnO/water (at 450 nm, or 2.76 eV) and Au-ZnO/water (at 560 nm, or 2.21 eV), respectively. The concentrated plasmonic E-field at the metal-semiconductor interface assists the transfer of the plasmon energy through the metal interband transition (single particle excitation) that enables excited electrons to readily overcome the Schottky barrier between the plasmonic metal and the semiconductor catalyst. This leads to hot electron injection from the plasmonic metal into the conduction band of the ZnO catalyst via plasmon excitation and decay.

In our work, the ZnO NWs were annealed to improve their donor concentrations[42] and reduce the Schottky barrier height of the ZnO-metal contacts, which resulted in high hot electron injection efficiency. This mechanism is illustrated in Fig. 7. The generated hot electrons then drift into the external circuit via the TCO contact, resulting in photocurrent generation under VIS light illumination, as shown in Fig. 4b. The minute current that was observed in the case of the pure-ZnO NW photoanode under VIS illumination (Fig. 4b) is possibly due to the marginal defect absorption of ZnO NWs by the deep donor level, as reported in the literature[30,31,41], which may be also combined with the VIS E-field enhancement that enhances the observed response.

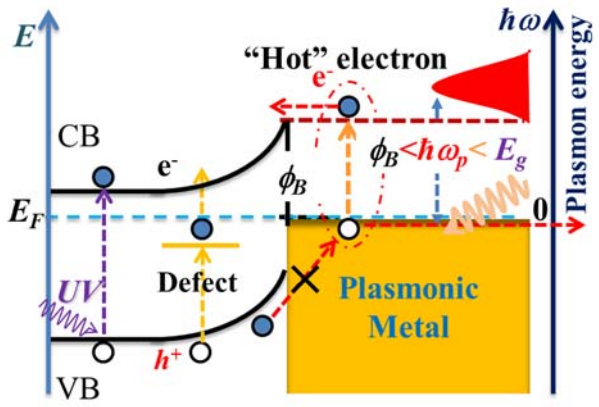

Fig. 6 Schematic illustration of mechanism for VIS photocatalytic activity of plasmonic metal-ZnO NWs caused by plasmon-induced hot electron.

The geometrical effects on plasmon-induced hot carrier injection from metal to semiconductor must be considered to achieve high quantum efficiency for the photoelectric transfer. These geometrical effects depend not only on the Schottky barrier height and the plasmon energy, but also on the momentum and the energy distributions of the generated hot carriers. One preferred geometry requires the hot carriers' momentum to contain a sufficiently large component in the direction perpendicular to the metal-semiconductor interface, as well as the E-field component of the incident light[13,14,54,60]. However, the quantum confinement is also expected to provide a sufficiently broad momentum distribution for electronic excitation to make the hot electron generation process remarkably efficient for nano-sized metal clusters[53]. For our plasmonic metal-loaded ZnO catalysts, the small sized (~13 nm) AgNPs and AuNPs can provide high quantum efficiency via plasmon-induced hot carrier injection because of the broad momentum distribution associated with light excitation. As shown in Fig. 5, with E-field excitation perpendicular to the NP-ZnO interface, the free electrons are excited and move in parallel with the E-field vector, resulting in the highest possible electron density at the metal-semiconductor interfaces and the highest possible E-field for the plasmon at the same position, which represents ideal conditions to induce hot electron injection. When the E-field is exactly parallel to the NP-ZnO interface, the electrons are oscillated away from the ZnO surface and the induced E-field magnitude is weak (see *e.g.*, the top and bottom NPs in Fig. 5b, c, e, and f); this can result in a weak electron injection probability under this condition.

To determine suitable geometrical conditions for efficient excitation of the NP plasmons (thus yielding higher photocurrents), we performed electromagnetic simulations while varying the geometry and polarization of the incident light. We performed RCWA simulations to simulate the absorption when varying the direction of incidence and polarization of the light with respect to the NP-loaded ZnO NW arrays. Examples of these simulations are shown in Fig. 7, from which we could understand the optimal tilting angles of the NW arrays with respect to the substrate that would provide the highest optical density. With metal NP-loaded ZnO NWs, the plasmon absorption intensity strongly depends on the angle of incidence with a maximum at approximately 50 to 70° (corresponding to the nanowire tilt angle of approximately 20 to 30°). The band-edge absorption of ZnO also has a slight dependence on the angle of incidence, exhibiting a similar maximum in the 50 to 70° range. As a whole, this structure shows optimized absorption for both UV (ZnO band-edge absorption) and VIS (plasmon absorption) light at around 50 to 70°. This angle corresponds nicely with the average tilt angle of our ZnO nanowires, which were readily grown on the TCOs with the wet chemical synthesis method presented here.

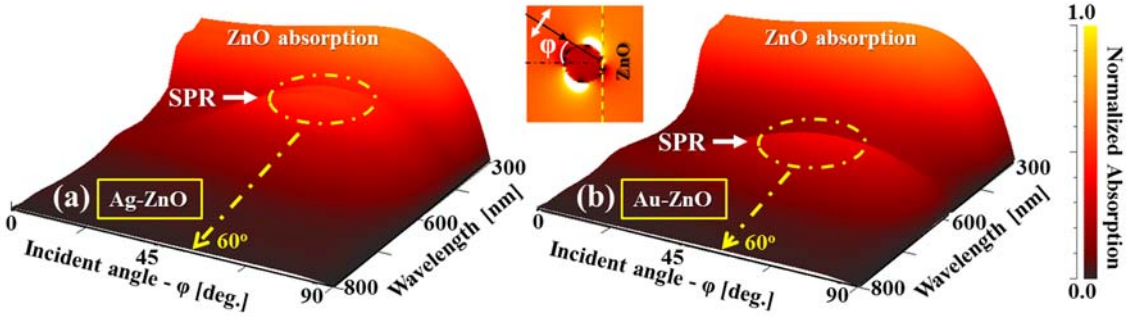

Fig. 7 Electromagnetic simulations of the incident angle-dependent absorption of plasmonic metal–ZnO NWs show the efficient absorption of the nanowire morphology with tilt angle: (a) AgNP-ZnO NW, and (b) AuNP-ZnO NW.

4. Conclusions

We have fabricated ZnO nanowire arrays loaded with noble metal nanoparticles by all-wet-chemical synthesis processes. These materials showed improved photocatalytic activity that was 2.4 to 3.2 times higher than that of a pristine ZnO NW arrays, which we clarified by degradation of MB molecules under sunlight illumination. The arrays showed promising performances in photoanode applications in a PEC cell, and we confirmed that they produced substantial photocurrents in both the UV region and the VIS region. The electromagnetic field calculations clarified the origin of the high optical density in the VIS region and provided optimal geometrical conditions that were suitable for high absorption of light in the UV to VIS region. The strong near-field enhancement at the NP-ZnO interface was also confirmed, showing in detail the microscopic mechanism responsible for the efficient hot carrier injection from metal to ZnO under VIS light illumination.

Combined plasmonic NP-semiconductor NW arrays such as those studied here have a wide variety of potential applications, ranging from solar-assisted photodegradation for environmental remediation to solar-assisted water splitting for hydrogen generation. We expect that the activity of this class of materials can be further improved by appropriate design of the electromagnetic near-field at the metal-oxide interface through electromagnetic simulations, along with careful selection of the constituent materials (oxides such as $SrTiO_3$, TiO_2, Fe_2O_3, and WO_3, combined with metals such as Pt, Ru, and Ni) via semiconductor band engineering. By combining this work with

nanophotonic design, band engineering, and control of the nano-architecture, *e.g.*, by further adapting the core-shell oxide heterojunction to efficiently promote carrier separation and reduce the carrier diffusion length[43], we will be able to further improve the photocatalytic performance of the proposed nanomaterials.

Acknowledgements

Part of this research was supported by a Grant-In-Aid for Scientific Research (no. 20671002) from JSPS.

References

1 K. Hashimoto, H. Irie and A. Fujishima, *Jpn. J. Appl. Phys.*, 2005, **44**, 8269.
2 S. R. Morrison, *J. Chem. Phys.*, 1967, **47**, 1543.
3 T. K. Townsend, N. D. Browning and F. E. Osterloh, *ACS Nano*, 2012, **6**, 7420–7426.
4 Y. Tian and T. Tatsuma, *J. Am. Chem. Soc.*, 2005, **127**, 7632–7637.
5 S. Linic, P. Christopher and D. B. Ingram, *Nat. Mater.*, 2011, **10**, 911–921.
6 P. Wang, B. Huang, Y. Dai and M.-H. Whangbo, *Phys. Chem. Chem. Phys.*, 2012, **14**, 9813.
7 X. Zhang, Y. L. Chen, R.-S. Liu and D. P. Tsai, *Rep. Prog. Phys.*, 2013, **76**, 046401.
8 K. Awazu, M. Fujimaki, C. Rockstuhl, J. Tominaga, H. Murakami, Y. Ohki, N. Yoshida and T. Watanabe, *J. Am. Chem. Soc.*, 2008, **130**, 1676–1680.
9 B. Iandolo, T. J. Antosiewicz, A. Hellman and I. Zorić, *Phys. Chem. Chem. Phys.*, 2013, **15**, 4947.
10 J. Li, S. K. Cushing, P. Zheng, F. Meng, D. Chu and N. Wu, *Nat. Commun.*, 2013, **4**.
11 M. Honda, Y. Kumamoto, A. Taguchi, Y. Saito and S. Kawata, *Appl. Phys. Lett.*, 2014, **104**, 061108.
12 M. W. Knight, H. Sobhani, P. Nordlander and N. J. Halas, *Science*, 2011, **332**, 702–704.
13 A. O. Govorov, H. Zhang and Y. K. Gun'ko, *J. Phys. Chem. C*, 2013, **117**, 16616–16631.
14 R. Sundararaman, P. Narang, A. S. Jermyn, W. A. Goddard III and H. A. Atwater, *Nat. Commun.*, 2014, **5**, 5788.
15 C. Clavero, *Nat. Photonics*, 2014, **8**, 95–103.
16 Y. Nishijima, K. Ueno, Y. Yokota, K. Murakoshi and H. Misawa, *J. Phys. Chem. Lett.*, 2010, **1**, 2031–2036.
17 A. Primo, A. Corma and H. García, *Phys. Chem. Chem. Phys.*, 2011, **13**, 886.
18 Z. Zhang, L. Zhang, M. N. Hedhili, H. Zhang and P. Wang, *Nano Lett.*, 2013, **13**, 14–20.
19 S. Mubeen, J. Lee, N. Singh, S. Krämer, G. D. Stucky and M. Moskovits, *Nat. Nanotechnol.*, 2013, **8**, 247–251.
20 L. Liu, T. D. Dao, R. Kodiyath, Q. Kang, H. Abe, T. Nagao and J. Ye, *Adv. Funct. Mater.*, 2014, **24**, 7754–7762.
21 C. Su, L. Liu, M. Zhang, Y. Zhang and C. Shao, *CrystEngComm*, 2012, **14**, 3989.
22 F. P. García de Arquer, A. Mihi, D. Kufer and G. Konstantatos, *ACS Nano*, 2013, **7**, 3581–3588.
23 Y. Zhong, K. Ueno, Y. Mori, X. Shi, T. Oshikiri, K. Murakoshi, H. Inoue and H. Misawa, *Angew. Chem.*, 2014, **126**, 10518–10522.
24 Y. Zheng, C. Chen, Y. Zhan, X. Lin, Q. Zheng, K. Wei and J. Zhu, *J. Phys. Chem. C*, 2008, **112**, 10773–10777.
25 R. Y. Hong, J. H. Li, L. L. Chen, D. Q. Liu, H. Z. Li, Y. Zheng and J. Ding, *Powder Technol.*, 2009, **189**, 426–432.
26 S. Gao, X. Jia, S. Yang, Z. Li and K. Jiang, *J. Solid State Chem.*, 2011, **184**, 764–769.
27 P. Fageria, S. Gangopadhyay and S. Pande, *RSC Adv.*, 2014, **4**, 24962.
28 F. Xu, Z.-Y. Yuan, G.-H. Du, T.-Z. Ren, C. Bouvy, M. Halasa and B.-L. Su, *Nanotechnology*, 2006, **17**, 588–594.
29 Q. Wang, B. Geng and S. Wang, *Environ. Sci. Technol.*, 2009, **43**, 8968–8973.
30 T. Jia, W. Wang, F. Long, Z. Fu, H. Wang and Q. Zhang, *J. Alloys Compd.*, 2009, **484**, 410–415.
31 D. Jian, P.-X. Gao, W. Cai, B. S. Allimi, S. Pamir Alpay, Y. Ding, Z. L. Wang and C. Brooks, *J. Mater. Chem.*, 2009, **19**, 970.
32 H. M. Chen, C. K. Chen, C.-J. Chen, L.-C. Cheng, P. C. Wu, B. H. Cheng, Y. Z. Ho, M. L. Tseng, Y.-Y. Hsu, T.-S. Chan, J.-F. Lee, R.-S. Liu and D. P. Tsai, *ACS Nano*, 2012, **6**, 7362–7372.
33 Y. L. Chen, L.-C. Kuo, M. L. Tseng, H. M. Chen, C.-K. Chen, H. J. Huang, R.-S. Liu and D. P. Tsai, *Opt. Express*, 2013, **21**, 7240–7249.
34 C. Wu, L. Shen, Y.-C. Zhang and Q. Huang, *Mater. Lett.*, 2011, **65**, 1794–1796.
35 Y. Zhang, M. K. Ram, E. K. Stefanakos and D. Y. Goswami, *Surf. Coat. Technol.*, 2013, **217**, 119–123.
36 J. M. Wu and W. T. Kao, *J. Phys. Chem. C*, 2015, 150112093320008.
37 C. Ren, B. Yang, M. Wu, J. Xu, Z. Fu, Y. lv, T. Guo, Y. Zhao and C. Zhu, *J. Hazard. Mater.*, 2010, **182**, 123–129.
38 T. Wang, Z. Jiao, T. Chen, Y. Li, W. Ren, S. Lin, G. Lu, J. Ye and Y. Bi, *Nanoscale*, 2013, **5**, 7552.
39 H. M. Chen, C. K. Chen, M. L. Tseng, P. C. Wu, C. M. Chang, L.-C. Cheng, H. W. Huang, T. S. Chan, D.-W. Huang, R.-S. Liu and D. P. Tsai, *Small*, 2013, **9**, 2926–2936.
40 X. Zhang, Y. Liu and Z. Kang, *ACS Appl. Mater. Interfaces*, 2014, **6**, 4480–4489.
41 W. Wu, G. Hu, S. Cui, Y. Zhou and H. Wu, *Cryst. Growth Des.*, 2008, **8**, 4014–4020.
42 S. Brochen, C. Granier, G. Feuillet and J. Pernot, *Appl. Phys. Lett.*, 2012, **100**, 052115.
43 T. D. Dao, C. T. T. Dang, G. Han, C. V. Hoang, W. Yi, V. Narayanamurti and T. Nagao, *Appl. Phys. Lett.*, 2013, **103**, 193119.
44 L. Mulfinger, S. D. Solomon, M. Bahadory, A. V. Jeyarajasingam, S. A. Rutkowsky and C. Boritz, *J. Chem. Educ.*, 2007, **84**, 322.
45 J. Kimling, M. Maier, B. Okenve, V. Kotaidis, H. Ballot and A. Plech, *J. Phys. Chem. B*, 2006, **110**, 15700–15707.
46 L. Schmidt-Mende and J. L. MacManus-Driscoll, *Mater. Today*, 2007, **10**, 40–48.
47 R. Ning, S. Wang, J. Wu, F. Wang and J.-M. Lin, *Small*, 2014, **10**, 4113–4117.
48 E. D. Palik, *Handbook of optical constants of solids*, Academic press, 1998, vol. 3.
49 H. Yoshikawa and S. Adachi, *Jpn. J. Appl. Phys.*, 1997, **36**, 6237–6243.
50 A. Houas, H. Lachheb, M. Ksibi, E. Elaloui, C. Guillard and J.-M. Herrmann, *Appl. Catal. B Environ.*, 2001, **31**, 145–157.
51 M. R. Hoffmann, S. T. Martin, W. Choi and D. W. Bahnemann, *Chem. Rev.*, 1995, **95**, 69–96.
52 M. Liu, C.-Y. Nam, C. T. Black, J. Kamcev and L. Zhang, *J. Phys. Chem. C*, 2013, **117**, 13396–13402.
53 A. O. Govorov, H. Zhang and Y. K. Gun'ko, *J. Phys. Chem. C*, 2013, **117**, 16616–16631.
54 R. H. Fowler, *Phys. Rev.*, 1931, **38**, 45.
55 H. B. Michaelson, *J. Appl. Phys.*, 1977, **48**, 4729.
56 D. Look, G. Farlow, P. Reunchan, S. Limpijumnong, S. Zhang and K. Nordlund, *Phys. Rev. Lett.*, 2005, **95**.
57 K. Jacobi, G. Zwicker and A. Gutmann, *Surf. Sci.*, 1984, **141**, 109–125.
58 S. Brochen, C. Granier, G. Feuillet and J. Pernot, *Appl. Phys. Lett.*, 2012, **100**, 052115.
59 R. M. Sheetz, E. Richter, A. N. Andriotis and M. Menon, *Phys. Rev. B*, 2009, **80**.
60 P. J. Schuck, *Nat. Nanotechnol.*, 2013, **8**, 799–800.

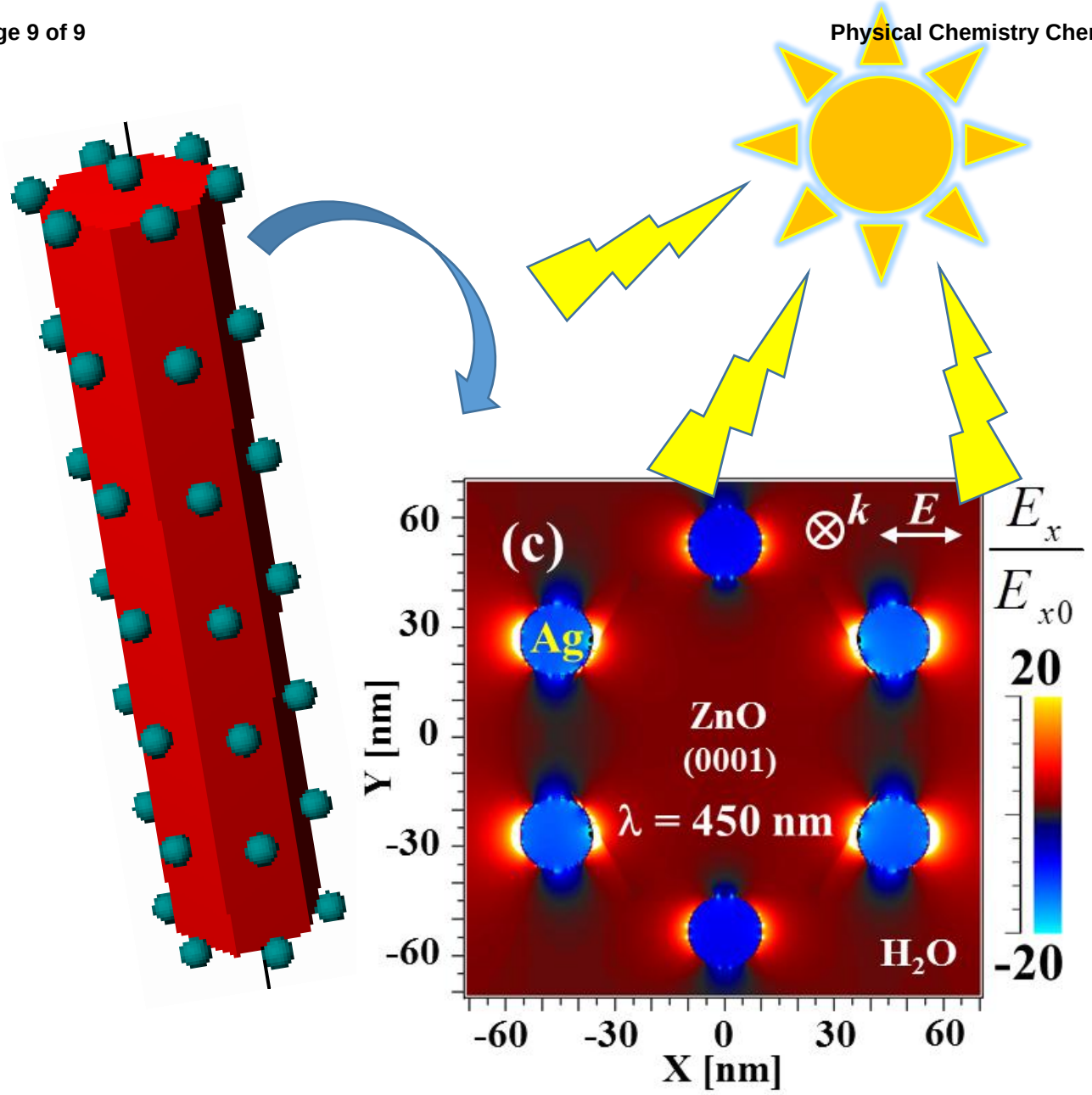

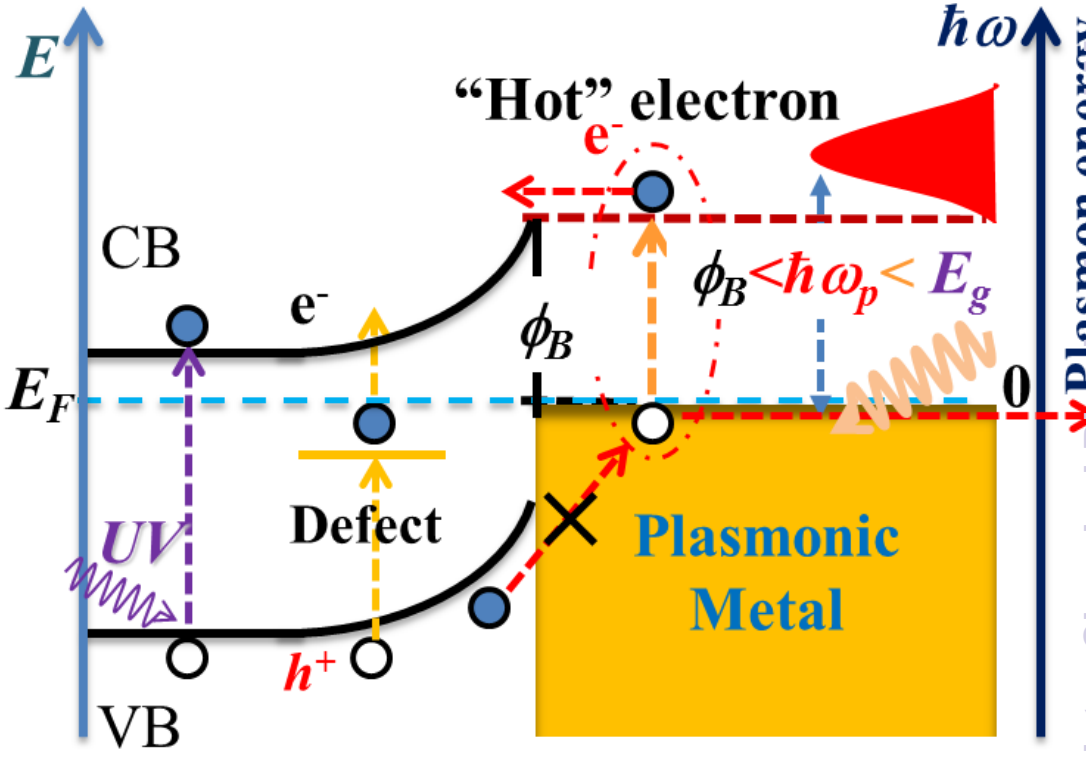

TOC T.D. DAO et al.

Relation among 1) photocatalytic activity 2) nano-scale electromagnetic field distribution and 3) hot electron injection of metal loaded ZnO wires was elucidated.